

UC Berkeley

UC Berkeley Previously Published Works

Title

Canted standing spin-wave modes of permalloy thin films observed by ferromagnetic resonance

Permalink

<https://escholarship.org/uc/item/1z25b8ck>

Journal

New Journal of Physics, 23(2)

ISSN

1367-2630

Authors

Dąbrowski, Maciej
Hicken, Robert J
Frisk, Andreas
et al.

Publication Date

2021-02-01

DOI

10.1088/1367-2630/abdd6b

Peer reviewed

PAPER • OPEN ACCESS

Canted standing spin-wave modes of permalloy thin films observed by ferromagnetic resonance

To cite this article: Maciej Dbrowski *et al* 2021 *New J. Phys.* **23** 023017

View the [article online](#) for updates and enhancements.



PAPER

Canted standing spin-wave modes of permalloy thin films observed by ferromagnetic resonance

OPEN ACCESS

RECEIVED

31 October 2020

REVISED

9 January 2021

ACCEPTED FOR PUBLICATION

19 January 2021




PUBLISHED

12 February 2021

Original content from this work may be used under the terms of the [Creative Commons Attribution 4.0 licence](https://creativecommons.org/licenses/by/4.0/).

Any further distribution of this work must maintain attribution to the author(s) and the title of the work, journal citation and DOI.



Maciej Dąbrowski^{1,*} , Robert J Hicken¹, Andreas Frisk² , David G Newman¹ ,
Christoph Klewe³, Alpha T N'Diaye³, Padraic Shafer³, Gerrit van der Laan²,
Thorsten Hesjedal⁴  and Graham J Bowden⁵

¹ Department of Physics and Astronomy, University of Exeter, Stocker Road, EX4 4QL, United Kingdom

² Diamond Light Source, Harwell Science and Innovation Campus, Didcot, OX11 0DE, United Kingdom

³ Advanced Light Source, Lawrence Berkeley National Laboratory, Berkeley, 94720, United States of America

⁴ Department of Physics, Clarendon Laboratory, University of Oxford, OX1 3PU, United Kingdom

⁵ School of Physics and Astronomy, University of Southampton, SO17 1BJ, United Kingdom

* Author to whom any correspondence should be addressed.

E-mail: m.k.dabrowski@exeter.ac.uk

Keywords: ferromagnetic resonance, standing spin waves, XFMR, canted magnetization, exchange spring magnet

Abstract

Non-collinear spin structures in materials that combine perpendicular and in-plane magnetic anisotropies are of great technological interest for microwave and spin wave-assisted magnetization switching. [Co/Pt] multilayers are well-known perpendicular anisotropy materials that have the potential to pin the magnetization of a soft magnetic layer, such as permalloy (Py), that has in-plane anisotropy, thereby forming a magnetic exchange spring. Here we report on multilayered [Co/Pt]/Pt/Py films, where an additional ultrathin Pt spacer has been included to control the coupling between the sub-units with in-plane and perpendicular magnetic anisotropy. Vector network analyser (VNA)-ferromagnetic resonance (FMR) measurements were made to obtain a complete picture of the resonant conditions, while the dynamical response of the sub-units was probed by synchrotron-based element- and phase selective x-ray detected FMR (XFMR). For all samples, only slight pinning of the dynamic magnetization of the Py by the [Co/Pt] was noted, and the FMR results were dominated by the 50 nm thick Py layer. Out-of-plane VNA-FMR maps reveal the presence of additional modes, e.g. a perpendicular standing spin-wave (PSSW) state. However, as the magnetic field is reduced below the saturation field, the PSSW state morphs continuously through a series of canted standing spin-wave (CSSW) states into a horizontal standing spin-wave (HSSW) state. The PSSW, CSSW and HSSW states are well described using a multilayer model of the Py film. The observation of CSSW modes is of particular relevance to microwave assisted magnetic recording, where microwave excitation stimulates precession of a soft layer canted out of plane by a pulsed magnetic field.

1. Introduction

The topic of ferromagnetic resonance (FMR) in thin magnetic films has a long, evolving history reaching back to Griffiths [1] and Kittel [2–6]. Studies employing FMR-based techniques have been crucial for gaining a deeper understanding of spin waves [7, 8]—a key component of novel microwave and spintronic devices, and for the design of high-speed, high-density magnetic memory [9–11]. Microwave devices based on the electromagnetic characteristics of spin waves, such as magnetic tunable filters, frequency multipliers, and signal-to-noise ratio enhancers, are widely used in radio frequency and microwave circuits [11]. Using vector network analyser (VNA)-FMR, a complete picture of resonant conditions in the form of two-dimensional maps, i.e. in the frequency vs applied field domain, can be obtained [12–14]. Combined with synchrotron radiation techniques, element- and phase selective x-ray detected FMR (XFMR) allows the properties of thin multilayer films to be probed layer-by-layer [15–19], and time-resolved scanning

transmission x-ray microscopy (STXM)-FMR enables the real-space imaging of the precessing magnetization in FMR down to a lateral resolution of several tens of nm [20]. In parallel, different advanced methods, such as Brillouin light scattering [21] and magneto-optical Kerr-effect microscopy [22] have been refined to allow for the high-resolution real-space imaging of spin wave modes in thin films and patterned elements.

One of the most thoroughly explored resonant spin wave modes in magnetic films is the perpendicular standing spin wave (PSSW) [6, 13, 14]. Regarding metallic ferromagnetic layers, $\text{Ni}_{80}\text{Fe}_{20}$ (permalloy, Py) has been a model system for studies of PSSW states, either in single layers [6, 23, 24], or in films coupled to adjacent ferromagnetic [25–28], or antiferromagnetic layers [29]. In general, the formation of PSSWs requires either nonuniform excitation or pinning of the magnetization. Using a coplanar waveguide (CPW) or a microstrip transducer, eddy-current shielding in conducting films results in nonuniform excitation across the magnetic film thickness, allowing for the formation of PSSWs [23, 26–28]. Alternatively, if the magnetization is pinned at one or both interfaces, PSSWs can be excited even with uniform microwave fields [5, 6]. In general, nonuniform excitation and pinning of the magnetization can be both present at the same time, making the observation of PSSWs sensitive to the experimental details and the characteristics of the particular magnetic stack. Efficient excitation and detection of PSSWs can also be achieved with laser pulses [30].

The motivation for this study is the detection of spin waves in non-collinear spin structures that combine perpendicular and in-plane magnetic anisotropy [31]. Such hybrid structures are still relatively unexplored, and yet, are of great technological interest from the viewpoint of microwave and spin wave-assisted magnetization switching [32]. A canted magnetization state allows the power consumption of spin-transfer-torque magnetic random-access memory (STT-MRAM) to be reduced [33], while microwave assisted magnetic recording (MAMR) in exchange springs systems involves the excitation of precession in magnetic layers that have their magnetization canted by a pulsed magnetic field. A full understanding of the switching process therefore requires knowledge of the normal modes of the canted state. We present both VNA-FMR and XFMR results on $\text{Py}(50)$, $[\text{Co}(0.4)/\text{Pt}(0.9)]_{10}/\text{Py}(50)$, $[\text{Co}(0.4)/\text{Pt}(0.9)]_{10}/\text{Pt}(1.5)/\text{Py}(50)$, and $[\text{Co}(0.4)/\text{Pt}(0.9)]_{10}/\text{Pt}(3)/\text{Py}(50)$ samples grown on an Al_2O_3 substrates (numbers in parentheses indicate thicknesses in nm, throughout this paper). The [Co/Pt] multilayer was selected, because it is characterized by perpendicular anisotropy [34]. In principle therefore, the [Co/Pt] has the potential to pin the bottom layers of the Py film, thereby allowing the formation of soft magnetic exchange springs in the 50 nm Py layer [31, 35]. Also, in an attempt to modify magnetic exchange across the interface, a thin Pt spacer, $t(\text{Pt}) = 0, 1.5, \text{ and } 3.0$ nm, was inserted between the Co/Pt substrate and Py, film. However, in practice it was found that the 50 nm Py layer dominated both the magnetic and FMR results. Nonetheless, the resulting 2D VNA-FMR maps reveal useful information, not only about the dominant uniform $\mathbf{k} = 0$ mode, but also about modes with $\mathbf{k} \neq 0$. In particular, one of Weber's PSSW modes [6] is identified, in fields applied normal to the film when $B_{\text{app}} > \mu_0 M = 1.0$ T. As expected, this PSSW state is characterized by a wavelength $\lambda = 2t$, where t is the thickness of the film. However, as the applied field is reduced below 1.0 T, the PSSW in question morphs into new canted spin-wave (CSSW) modes. The frequency of these modes increases as the field is reduced, until in zero field a horizontal standing spin-wave (HSSW) mode is reached, with a frequency of ~ 9.5 GHz. CSSW and HSSW modes therefore correspond to the magnetization orientations in the canted and the in-plane state, respectively. Please note that all the observed standing spin wave states are formed with the wavevectors of the constituent counter-propagating waves aligned along the surface normal direction, and are PSSWs in the traditional sense of the term. However, to distinguish between different characteristics of standing spin waves with different orientations of the magnetization, here we introduce terms HSSW, CSSW and PSSW.

The structure of this paper is as follows. In section 2, 2D VNA-FMR maps for the different [Co/Pt]/Py samples in question, are presented and discussed. This is followed in sections 3 and 4 by a theoretical discussion, where the FMR *master equation* for a single slab of Py is examined, for fields applied at an arbitrary angle with respect to the normal to the film. In particular, special attention is paid to the case where the field is applied perpendicular to the film, and slightly off the perpendicular. This misalignment turns out to be important for the interpretation of out-of-plane FMR results. We use the term *master equation*, because it is this equation which allows us to determine not only the 'equilibrium state', but also the 'elementary excitations', using the process of 'linearization'. The actual linearization procedure used here is primarily *quantum mechanical*, following van Vleck [36] and Nörtemann *et al* [37]. Nonetheless, the results mirror (i) the classical approach of e.g. Gurevich and Melkov [38], based on the famous Landau–Lifshitz–Gilbert equation (e.g. Gilbert [39]), and (ii) the free-energy method (e.g. Smit & Beljers [40], Farle [41]).

In sections 5–7, we turn our attention to the excited states $k \neq 0$. In particular, we identify a PSSW in the VNA-FMR map, in the out-of-plane field measurements when $B_{\text{app}} > \mu_0 M$. This state manifests itself

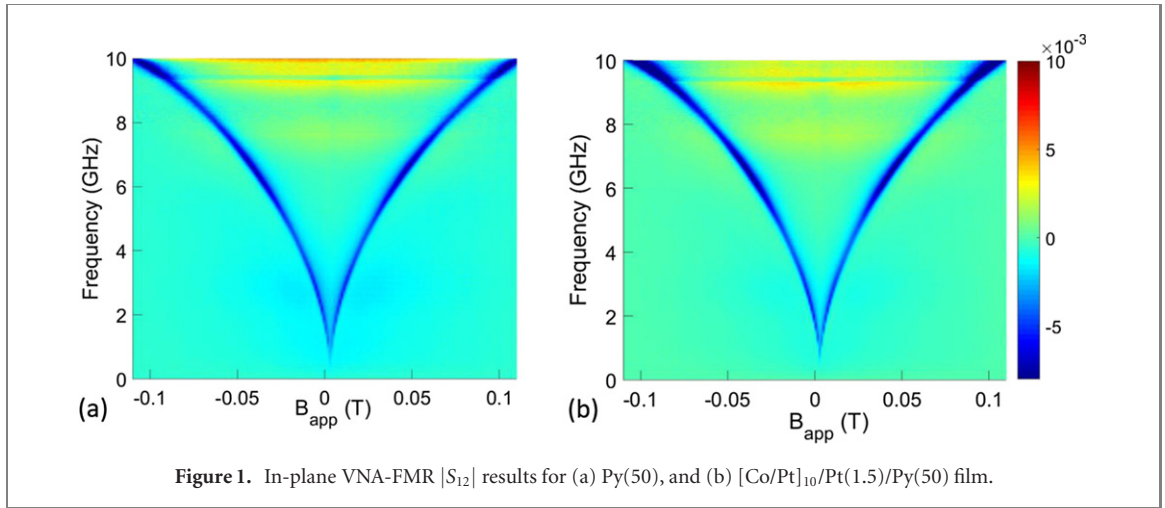


Figure 1. In-plane VNA-FMR $|S_{12}|$ results for (a) Py(50), and (b) [Co/Pt]₁₀/Pt(1.5)/Py(50) film.

as a line running parallel to that of the uniform $k = 0$ FMR mode. However, in the low field region $\mu_0 M \geq B_{\text{app}} \geq 0$, the PSSW mode morphs into an HSSW mode, rising up in frequency to ~ 9.45 GHz at $B_{\text{app}} = 0$. It is shown that this behaviour can be understood in terms of a multilayer Py model, based on the linearization method used by Nörtemann *et al* [37], but modified to include the layer-by-layer local dipolar field approach of Bowden *et al* [42]. The results are in good agreement with the excited states observed in both 50 nm Py and 100 nm Py films. In addition, the *ellipticity* of FMR precession is highlighted and discussed.

Finally, in section 8, we summarize our results and give suggestions for further exploration.

2. Experimental results

The samples were deposited on Al₂O₃ substrates at room temperature using dc magnetron sputtering. The films were grown on a Pt(30) seed layer and capped with a Pt(3) protective layer. The VNA-FMR measurements were performed on a standard CPW with 50 Ω impedance and with a signal line of 500 μm width. An electromagnet mounted on a rotating stage supplied a bias magnetic field either in the sample plane or normal to the sample plane. The measurements were performed by stepping the magnetic field value and sweeping the microwave frequency in the range 0–20 GHz. The samples were placed face down, with the magnetic layers in close proximity to the CPW. For each applied magnetic field value, a reference measurement was made at high field and subtracted in order to remove the background signal. The in-plane VNA-FMR frequency vs applied field map for the 50 nm thick Py reference sample and [Co/Pt]₁₀/Pt(1.5)/Py(50) film can be seen in figure 1, where the colour scale represents $|S_{12}|$ the magnitude of the measured scattering matrix parameter. In general, the FMR lines for all investigated samples look very similar and follow the expected behaviour for a simple Py film. For directly coupled samples (without a Pt spacer layer) and with thinner Py thicknesses (< 50 nm), the results of VNA-FMR measurements change substantially, due to the formation of an imprinted domain and exchange spring structure [43]. Note that the FMR of [Co/Pt] is generally out of range for our setup in terms of accessible frequency/field values [34].

The data shown in figure 1 can be fitted with the usual Kittel formula:

$$\nu = \gamma \sqrt{(B_{\text{app}} + |B_K|) (B_{\text{app}} + |B_K| + \mu_0 M)}. \quad (1)$$

Here, (i) $\gamma = 29.4$ GHz T⁻¹, (ii) $\mu_0 M = 1.0$ T for Py, and (iii) B_K is a small in-plane anisotropy field, which gives rise to the small gap $\nu \sim 0.5$ GHz in zero applied field. From the latter we find $B_K \sim 0.0003$ T (favouring an in-plane axis).

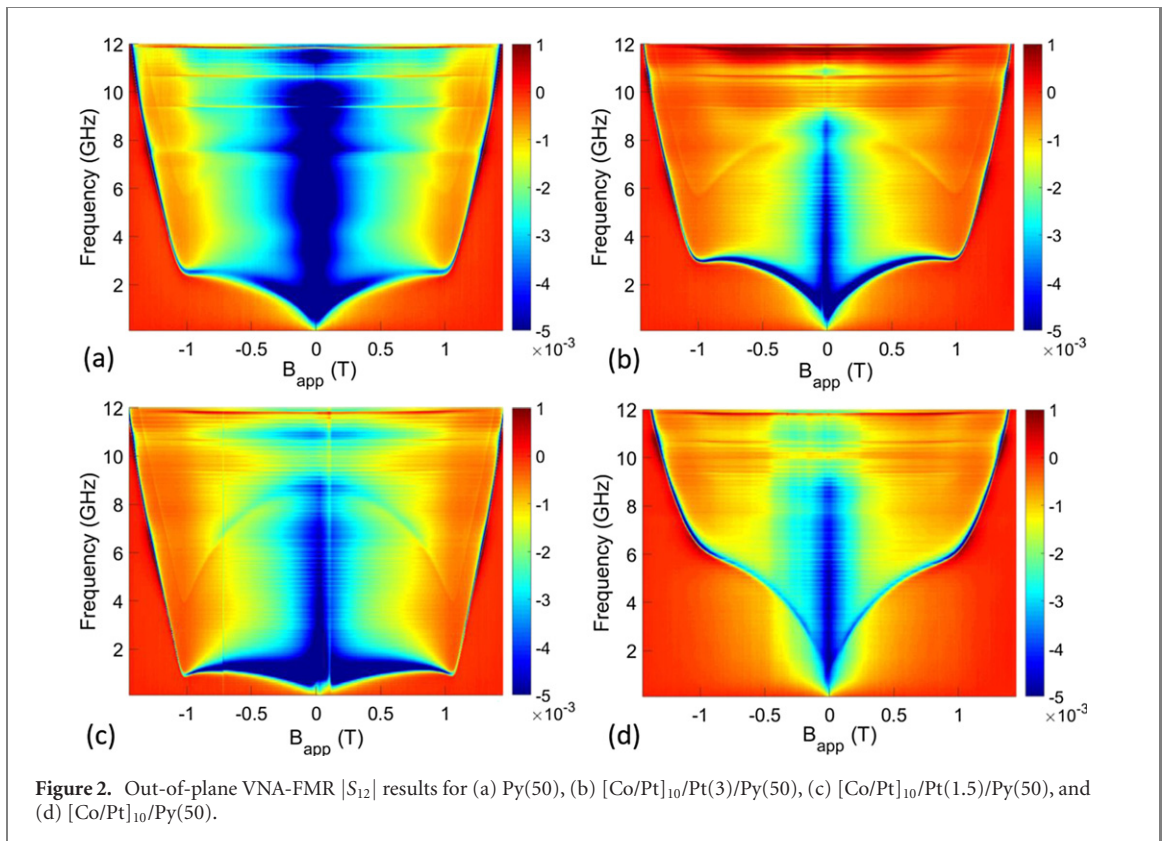
The out of plane FMR results, for the four samples in question, can be seen in figure 2. Note the ten-fold increase in the magnetic field on going from the in-plane to out-of-plane FMR results.

Using Kittel's formula for out-of-plane FMR (in the absence of any crystal field interactions) we expect:

$$\nu = 0 \quad \text{for } 0 \leq B_{\text{app}} \leq \mu_0 M.$$

$$\nu = \gamma (B_{\text{app}} - \mu_0 M) \quad \text{for } B_{\text{app}} > \mu_0 M. \quad (2)$$

In general, for fields in excess of the saturation magnetization $\mu_0 M = 1.0$ T there is a sharp linear rise in the FMR frequency, as expected. However, for fields below 1.0 T, the FMR frequency is certainly non-zero, and



is characterized by a sharp *cusp* at $B_{\text{app}} \sim 1.0$ T (see in particular figure 2(c)). Note that the strong absorption below $B_{\text{app}} \sim |0.2|$ T is a background signal arising from the CPW and coaxial cables.

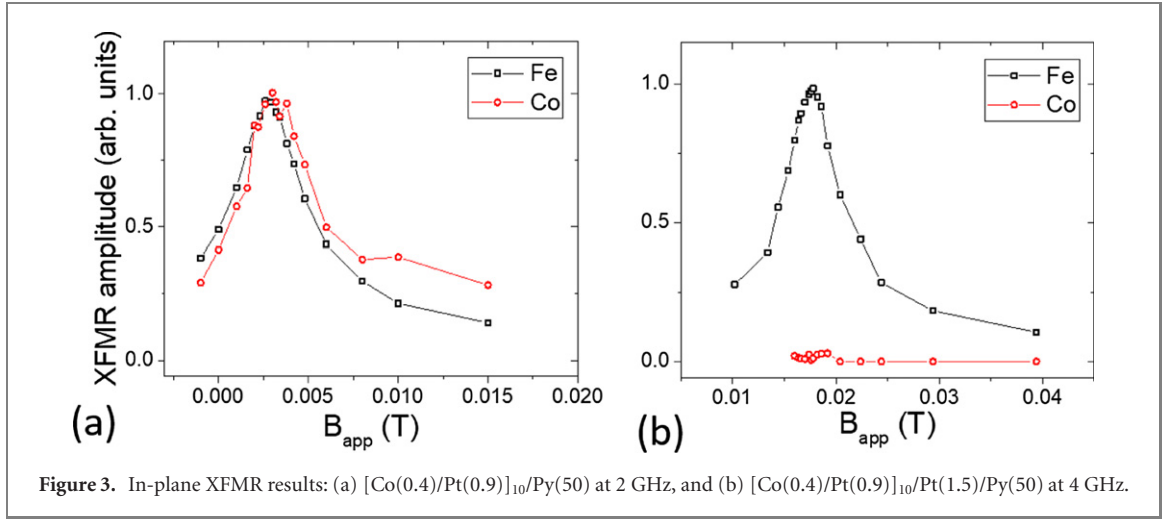
In the following section, we provide an explanation of many of the features seen in figure 2. However before leaving this experimental section, consider also the results of XFMR experiments [15, 16, 44, 45]. XFMR measurements were carried out on beamline 4.0.2 of the advanced light source by monitoring absorption/transmission as a function of time delay between a synchronized RF magnetic field (pumping the spin precession) and circularly polarized x-ray pulses (probing the oscillatory magnetization component along the x-ray wavevector). The x-rays were incident at a grazing angle of 40° . The sample was placed face down on a CPW with a countersunk hole of $500 \mu\text{m}$ diameter allowing the incident x-ray beam to access the surface of the sample, while the transmitted x-rays were converted to optical radiation through x-ray excited optical luminescence in the Al_2O_3 substrate, with the emitted light detected by a photodiode mounted behind the sample.

By tuning the x-ray energy to the absorption edge of the element of interest, the XFMR signals from the Py (Fe L_3 edge) and [Co/Pt] (Co L_3 edge) were detected separately, allowing direct measurement of the FMR within each layer. Both the amplitude and phase of precession were extracted by fitting a sine wave to the XFMR delay scans. The amplitudes of the Fe and Co moments, normalized to their static XMCD signals are shown for two samples [Co/Pt]₁₀/Py(50) and [Co/Pt]₁₀/Pt(1.5)/Py(50), in figures 3(a) and (b), respectively. While for directly coupled layers both [Co/Pt] and Py precess with the same amplitude, it is clear that the Co spins in the [Co/Pt] layer and the Fe spins in the Py film are dynamically *decoupled* when the Pt spacer exceeds 1.5 nm; thereby providing extra justification for our earlier general statement that the FMR results appear to be dominated by the 50 nm Py film alone. The sole exception appears to be that of the directly coupled [Co/Pt]/Py film shown in figure 2(d), where the *cusp* in the FMR rises to ~ 6 GHz. Initially, it was believed that such behaviour could signal the presence of an exchange spring. However, in the sections 3 and 4 below, a totally different interpretation of figure 2(d), is presented and discussed.

3. Quantum mechanical description of FMR: single slab

In this section, we concentrate primarily on the *out-of-plane* results presented in figure 2.

The right-handed coordinate system used in this work can be seen in the inset of figure 4. Initially, the magnetization should lie along the *in-plane* x-axis, due to (i) the strong demagnetization factor associated with the *out-of-plane* z-axis, and (ii) a small in-plane anisotropy, discussed earlier. However, when the field



is applied along the z -axis the magnetization will rotate out-of-plane making an angle θ with respect to the z -axis.

Next, we follow the quantum mechanical approach pioneered by Van Vleck [36]. Here, the magnetization is envisaged as a single spin \mathbf{J} , much in the way of Kittel [3]. We adopt this approach, because it paves the way for a multilayer model (section 6), where the spins are coupled through a Heisenberg exchange interaction.

The time dependence of the angular momentum operator \mathbf{J} is given by;

$$\frac{d}{dt} \langle \mathbf{J} \rangle = -\frac{i}{\hbar} \langle [\mathbf{J}, \mathcal{H}]_- \rangle. \quad (3)$$

Here \mathcal{H} is the Hamiltonian, and the angular momentum \mathbf{J} is assumed dimensionless. Thus, the necessary commutation relationships, used to evaluate equation (3), take the form $[J_x, J_y]_- = iJ_z$ etc.

For the Py film in question, the Hamiltonian is given by:

$$\mathcal{H} = \mathcal{H}_{\text{ZM}} + \mathcal{H}_{\text{A}} + \mathcal{H}_{\text{Loc}}. \quad (4)$$

The individual terms are as follows. The Zeeman (ZM) interaction:

$$\mathcal{H}_{\text{ZM}} = -\boldsymbol{\mu} \cdot \mathbf{B}_{\text{app}} = -g\mu_{\text{B}} \mathbf{J}_k \cdot \mathbf{B}_{\text{app}} = -g\mu_{\text{B}} J_z B_{\text{app}}^z. \quad (5)$$

The crystal field Hamiltonian:

$$\mathcal{H}_{\text{A}} = K_{\text{A}} \left(J_x^2 - \frac{1}{3} J(J+1) \right). \quad (6)$$

(Note that the anisotropy parameter K_{A} must be negative to favour the in-plane x -axis.)

The dipolar field contribution arising from all the dipoles in the film takes the form:

$$\mathcal{H}_{\text{Loc}} = -\boldsymbol{\mu} \cdot \mathbf{B}_{\text{Loc}} = -g\mu_{\text{B}} \mathbf{J} \cdot \mathbf{B}_{\text{Loc}}. \quad (7)$$

Here:

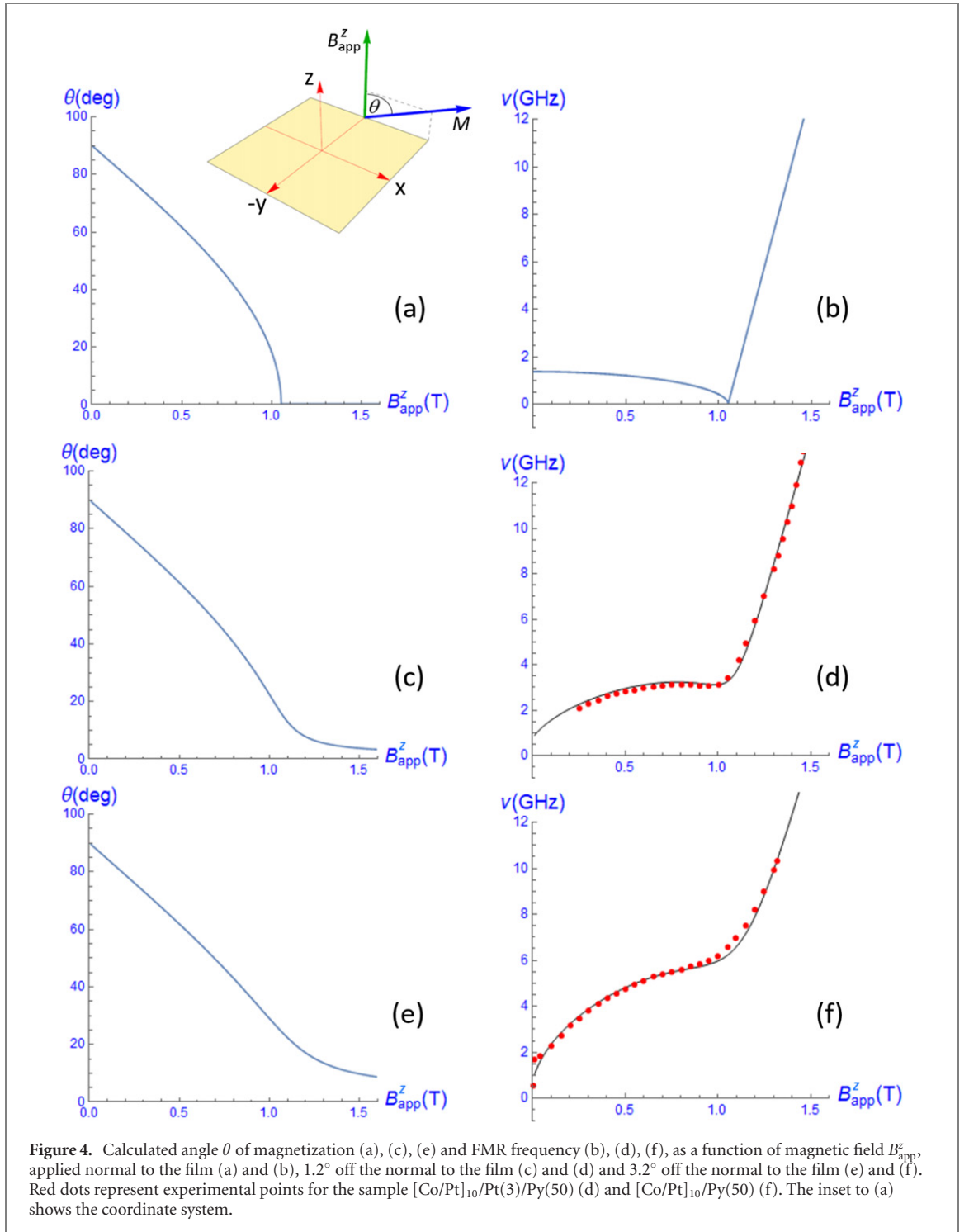
$$\mathbf{B}_{\text{Loc}} = \frac{B_{\text{Lor}}}{\mu} \begin{pmatrix} 1 & 0 & 0 \\ 0 & 1 & 0 \\ 0 & 0 & -2 \end{pmatrix} \begin{pmatrix} \mu_x \\ \mu_y \\ \mu_z \end{pmatrix}; \quad B_{\text{Lor}} = \frac{\mu_0 M}{3}. \quad (8)$$

Note that equation (8) contains *both* the demagnetizing term and the Lorentz field. Some readers may question this approach, given that the Lorentz field *per se* cannot contribute to the torque on the magnetization of the slab. However, in sections 5 and 6, we generalize the single slab model discussed here, to a multilayer model. In the latter, the Lorentz field $\frac{\mu_0 M}{3}$, only holds if the spins of all the layers are collinear (see Bowden *et al* [42]). Thus, for both $k \neq 0$ standing spin wave modes and exchange springs, it is necessary to generalise equation (8). Finally, we note that while the above QM approach holds only for $T = 0$ K, the results obtained by this method are the same as those given by Kittel.

For the Zeeman interaction, anisotropy, and local dipolar field contributions, in question, we find:

(i):

$$-\frac{i}{\hbar} \langle [\mathbf{J}, \mathcal{H}_{\text{ZM}}]_- \rangle = \left(\frac{g\mu_{\text{B}}}{\hbar} \right) \langle \mathbf{J} \rangle \times \mathbf{B}_{\text{app}} = \left(\frac{g\mu_{\text{B}}}{\hbar} \right) B_{\text{app}}^z \left(J_y \hat{\mathbf{i}} - J_x \hat{\mathbf{j}} \right) \quad (9)$$



(ii):

$$-\frac{i}{\hbar} \langle [J, \mathcal{H}_A]_- \rangle = \left(\frac{K_A}{\hbar} \right) \left(-\langle [J_x, J_z]_+ \rangle \hat{j} + \langle [J_x, J_y]_+ \rangle \hat{k} \right). \quad (10)$$

(Note the presence of the anti-commutators.)

(iii):

$$-\frac{i}{\hbar} \langle [J, \mathcal{H}_{\text{Loc}}]_- \rangle = -\frac{i}{\hbar} \langle [J, -g\mu_B \mathbf{J} \cdot \mathbf{B}_{\text{Loc}}]_- \rangle = \left(\frac{g\mu_B}{\hbar} \right) \langle \mathbf{J} \rangle \times \mathbf{B}_{\text{Loc}}. \quad (11)$$

Next, we assume all the moments are in the z - x plane, at an angle θ with respect to the z -axis. Consequently:

$$\boldsymbol{\mu} = \begin{pmatrix} \mu_x \\ \mu_y \\ \mu_z \end{pmatrix} = \mu \begin{pmatrix} \sin \theta \\ 0 \\ \cos \theta \end{pmatrix}. \quad (12)$$

Thus:

$$\mathbf{B}_{\text{Loc}} = \frac{\mu_0 M}{3} \begin{pmatrix} \sin \theta \\ 0 \\ -2 \cos \theta \end{pmatrix}. \quad (13)$$

Summing up therefore:

$$\begin{aligned} \hbar \frac{d}{dt} \langle \mathbf{J} \rangle &= \boldsymbol{\mu} \times (\mathbf{B}_{\text{app}} + \mathbf{B}_{\text{Loc}}) + K_{\Lambda} \left(-\langle [J_x, J_z]_+ \rangle \hat{\mathbf{j}} + \langle [J_x, J_y]_+ \rangle \hat{\mathbf{k}} \right) \\ &= \mu \begin{pmatrix} \sin \theta \\ 0 \\ \cos \theta \end{pmatrix} \times \left(\begin{pmatrix} 0 \\ 0 \\ B_{\text{app}}^z \end{pmatrix} + \frac{\mu_0 M}{3} \begin{pmatrix} \sin \theta \\ 0 \\ -2 \cos \theta \end{pmatrix} \right) - 2K_{\Lambda} J^2 \sin \theta \cos \theta \begin{pmatrix} 0 \\ 1 \\ 0 \end{pmatrix}. \\ &= [\mu \sin \theta (-B_{\text{app}}^z + \mu_0 M \cos \theta - B_K \cos \theta)] \hat{\mathbf{j}}. \end{aligned} \quad (14)$$

Note that we have followed the usual convention in defining the anisotropy field:

$$B_K = \frac{+2K_{\Lambda}J}{g\mu_B}. \quad (15)$$

Alternatively, in terms of magnetic moments:

$$\begin{aligned} \frac{d}{dt} \langle \boldsymbol{\mu} \rangle &= \gamma [\mu \sin \theta (B_{\text{app}}^z - \mu_0 M \cos \theta + B_K \cos \theta)] \hat{\mathbf{j}}. \\ &\left(\gamma = \frac{g|\mu_B|}{h} \right). \end{aligned} \quad (16)$$

Equation (16) is the *master* equation, referred to earlier. Note that the torque is solely about the y -axis. We are now in a position to determine the equilibrium angle of magnetization θ , and hence the elementary ground state excitations.

In equilibrium, the torque must be zero. Thus:

$$\begin{aligned} \cos \theta &= \frac{B_{\text{app}}^z}{(\mu_0 M - B_K)} \quad (B_{\text{app}}^z < \mu_0 M - B_K). \\ \theta &= 0^{\circ} \quad (B_{\text{app}}^z \geq \mu_0 M - B_K). \end{aligned} \quad (17)$$

Next, we use the master equation (16), now equipped with the equilibrium angle θ , to determine the elementary excitations using the process known as linearization $\mu_x \rightarrow \mu_x^0 + d\mu_x e^{i\omega t}$ etc (see Van Vleck [36] and Nörtemann *et al* [37]). Here, the $d\mu_x$ etc, are small time-dependent deviations away from the equilibrium values. Thus, on collecting the first order terms (linearization), we find:

$$\begin{pmatrix} d\dot{\mu}_x \\ d\dot{\mu}_y \\ d\dot{\mu}_z \end{pmatrix} = -\gamma \left\{ B_{\text{app}}^z \begin{pmatrix} d\mu_y \\ -d\mu_x \\ 0 \end{pmatrix} + \mu_0 M \begin{pmatrix} -d\mu_y \cos \theta \\ d\mu_x \cos \theta + d\mu_z \sin \theta \\ 0 \end{pmatrix} + B_K \begin{pmatrix} 0 \\ -d\mu_x \cos \theta - d\mu_z \sin \theta \\ d\mu_y \sin \theta \end{pmatrix} \right\} \quad (19)$$

Or alternatively, in matrix form:

$$\begin{pmatrix} i\nu & \gamma (B_{\text{app}}^z - \mu_0 M \cos \theta) & 0 \\ -\gamma (B_{\text{app}}^z - \mu_0 M \cos \theta + B_K \cos \theta) & i\nu & \gamma (\mu_0 M \sin \theta - B_K \sin \theta) \\ 0 & \gamma B_K \sin \theta & i\nu \end{pmatrix} \begin{pmatrix} d\mu_x \\ d\mu_y \\ d\mu_z \end{pmatrix} = 0. \quad (20)$$

Consequently, we have a solution for $d\mu_x$ etc, provided:

$$\nu = \pm \gamma \sqrt{\frac{(B_{\text{app}}^z - \mu_0 M \cos \theta) (B_{\text{app}}^z - \mu_0 M \cos \theta + B_K \cos \theta)}{+B_K \sin^2 \theta (B_K - \mu_0 M)}}. \quad (21)$$

Some results for the Py(50) film can be seen in figures 4(a) and (b). In general, the excitation spectra in figure 4(b) replicate the general features found in the out-of-plane FMR results shown in figure 2. In particular, the presence of a small anisotropy field B_K ensures that the FMR frequency is non-zero for fields $B_{\text{app}}^z < \mu_0 M$.

However, the most striking feature of the FMR calculation of figure 4(b) is that of the sharp downturn in frequency (*cusp*), to zero, at $B_{\text{app}}^z = \mu_0 M - B_K$ (~ 1 T). We believe that this may be an example of the

Goldstone theorem: in a system with a continuous broken symmetry, there may exist excitations with arbitrary low energy. At the *cusp*, the spins approach the angle of 0° very rapidly. Explicitly:

$$\frac{d\theta}{dB_{\text{app}}^z} = \frac{1}{(\mu_0 M - B_K) \sin \theta}. \quad (22)$$

Consequently, as $\theta \rightarrow 0$, the derivative $\frac{d\theta}{dB_{\text{app}}^z} \rightarrow \infty$, and concomitantly $\omega \rightarrow 0$. In physical terms, the spins become very mobile at the *cusp*. Thus, it is energetically very easy to set-up a uniform $k = 0$ spin-wave. Alternatively, we can describe the above behaviour as a ‘soft-mode’. In this regard, we note that Kuanr *et al* [46] have reported soft mode behaviour, in nanosized Py strips. However, the latter gave no interpretation of their soft mode, which is not the same as that under discussion here.

On course, sharp features in any characteristic curve, invite mode mixing of one kind or another. However, before examining such possibilities (e.g. magnetostatic modes), it is probably wise to examine how the cusp behaves with slight misalignment of the applied field (applied along the normal to the plane). As we shall see, it turns out that alignment of the magnetic field perpendicular to the Py film is critical.

4. FMR with slight misalignment of out-of-plane applied field

First, we acknowledge that this problem has been addressed, many years ago, by Tannenwald and Seavey [47] (see their figure 2). However, the latter do not include an in-plane anisotropy. So, unlike figure 4(b) above, resonance was not observed by Tannenwald and Seavey [47], until the applied field B_{app}^z , normal to the plane, exceeds $\mu_0 M$.

Suppose the applied field is slightly misaligned in the z - x plane. The master equation (16) is transformed to:

$$\begin{aligned} \hbar \frac{d}{dt} \langle \mathbf{J} \rangle &= \mu \begin{pmatrix} \sin \theta \\ 0 \\ \cos \theta \end{pmatrix} \times \left(\begin{pmatrix} B_{\text{app}}^x \\ 0 \\ B_{\text{app}}^z \end{pmatrix} + \frac{\mu_0 M}{3} \begin{pmatrix} \sin \theta \\ 0 \\ -2 \cos \theta \end{pmatrix} \right) - 2K_A J^2 \sin \theta \cos \theta \begin{pmatrix} 0 \\ 1 \\ 0 \end{pmatrix} \\ &= [\cos \theta B_{\text{app}}^x - \sin \theta B_{\text{app}}^z + \sin \theta \cos \theta (\mu_0 M - B_K)] \hat{\mathbf{j}}. \end{aligned} \quad (23)$$

Thus, we have a new solution for the equilibrium angle, which requires a numerical solution:

$$\cos \theta B_{\text{app}}^x - \sin \theta B_{\text{app}}^z + \sin \theta \cos \theta (\mu_0 M - B_K) = 0. \quad (24)$$

Note that this solution readily reverts to that of equation (12), when $B_{\text{app}}^x = 0$.

Turning now to the dynamics we find:

$$\begin{aligned} &\begin{pmatrix} i\nu & \gamma (B_{\text{app}}^z - \mu_0 M \cos \theta) & 0 \\ -\gamma (B_{\text{app}}^z - \mu_0 M \cos \theta + B_K \cos \theta) & i\nu & \gamma (B_{\text{app}}^x + \mu_0 M \sin \theta - B_K \sin \theta) \\ 0 & -\gamma (B_{\text{app}}^x - B_K \sin \theta) & i\nu \end{pmatrix} \\ &\times \begin{pmatrix} d\mu_x \\ d\mu_y \\ d\mu_z \end{pmatrix} = 0. \end{aligned} \quad (25)$$

Consequently, we have a solution for $d\mu_x$ etc, provided:

$$\nu = \pm \gamma \sqrt{\frac{(B_{\text{app}}^z - \mu_0 M \cos \theta) (B_{\text{app}}^z - \mu_0 M \cos \theta + B_K \cos \theta)}{-(B_K \sin \theta - B_{\text{app}}^x) (B_{\text{app}}^x - B_K \sin \theta + \mu_0 M \sin \theta)}}. \quad (26)$$

The results of this calculation, for small misalignments of the applied field, can be seen in figures 4(c)–(d). From an examination of figure 4(c) we see that (i) the angle of magnetization θ never reaches 0° and (ii) the *cusp* in figure 4(d) does not dip down to zero near $B_{\text{app}}^z \approx \mu_0 M$. This fit was obtained with $B_K = -0.0007$ T, $\mu_0 M = 1.025$ T, $d\theta = 1.2^\circ$, and $\gamma = 29.4$ GHz T $^{-1}$. In addition, for negative B_{app}^x field (not shown), the magnetization reverses producing a mirror image of the data shown in figure 4(d).

In figures 4(e) and (f) we show the similar calculations to those of figures 4(c) and (d), in fact with the same parameters except that the misalignment is set at $d\theta = 3.3^\circ$. From an examination of figure 4(f) it is observed that the *cusp* is now much less sharp and has moved up to ~ 6 GHz. This behaviour replicates well, the out-of-plane VNA-FMR results for the [Co(0.4)/Pt(0.9)] $_{10}$ /Py(50) film.

In summary therefore, the out-of-plane VNA-FMR $k = 0$ mode results can be well-understood in terms of small misalignments of the applied field, with respect to the film normal. In appendix B more VNA-FMR diagrams can be seen, showing how the *cusp* changes with slight field adjustments about the normal to the film.

This completes our discussion of the $k = 0$ uniform mode. However, as noted earlier, the out-of-plane 2D VNA-FMR maps also contain additional information about $k \neq 0$ modes. However, before we examine these modes, it is advantageous to detail a multi-layer model of the Py film, which can be used to accurately model the properties of the PSSW, CSSW, and HSSW modes.

5. Multilayer Py model

Essentially, we follow the multilayer model described by Utsumiya *et al* [48] (and references therein), used to interpret the exchange spring behaviour in pinned $L1_0$ -FePt/Py exchange-spring films. However, we differ from former in that local dipolar fields are included, using the layer by layer model of Bowden *et al* [42]. In addition, we also make use of the ‘double differential energy matrix’ detailed by Bowden *et al* [49]. The eigenvalues of this matrix allow a quick identification of whether a particular energy state is stable or otherwise.

In general, the original master equation is now replaced by a matrix of coupled equations, which can be used to determine the equilibrium set of angles $\{\theta_i, \phi_i\}$. Once the latter are available, the elementary FMR excitations are subsequently determined using the linearization procedure of Nörtemann *et al* [37]. In addition, we make use of local variables, as opposed to an overall global Cartesian frame of reference. This approach confers two advantages. One, the number of incremental variables is reduced, from three variables $\{\partial\mu_x^i, \partial\mu_y^i, \partial\mu_z^i\}$ to just two per spin: $\{\partial\theta_i, \sin\theta_i\partial\phi_i\}$. Two, it is easy to determine the *ellipticity* of the precession of the spins, about their equilibrium positions.

First, we note that the single-particle terms, namely the Zeeman and the anisotropy interactions, have already been detailed [see equations (9) and (10), respectively]. Thus, we only need to consider terms that involve (i) magnetic exchange, and (ii) dipolar interactions between differing layers.

For thin films, with nearest neighbour interactions, we recast the exchange interaction \mathcal{H}_{Ex} into the 1D-planar form:

$$\mathcal{H}_{\text{Ex}} = \sum_{k=1}^n \mathcal{H}_{\text{Ex}}(k) \quad (27)$$

$$\mathcal{H}_{\text{Ex}}(k) = -\frac{1}{2}\lambda_{\text{ex}}(\mathbf{J}_k \cdot \mathbf{J}_{k+1} + \mathbf{J}_k \cdot \mathbf{J}_{k-1}) - \lambda_{\text{ex}} \sum_{\rho=1}^4 \mathbf{J}_k \cdot \mathbf{J}_{k+\rho}. \quad (28)$$

Here, we make the following assumptions: (i) The spins occupy a cubic lattice. (ii) The integer k defines a plane within the thin film (along the z -axis normal to the plane of the film). (iii) All the spins within a plane (k -fixed, $\rho = 1, 4$) are parallel $\mathbf{J}_k \parallel \mathbf{J}_{k+\rho}$. (iv) Only the nearest-neighbour interactions are included. Note that the inclusion of the factor 1/2 avoids double counting. However, slight modifications are necessary at the top and bottom layers of the film. Finally, if all the spins are parallel, the exchange term reduces to $\mathcal{H}_{\text{Ex}}(k) = -6\lambda_{\text{ex}}J^2$, as expected.

For the magnetic exchange we find:

$$\left(\frac{d}{dt} \langle \mathbf{J}_k \rangle\right)_{\text{Ex}} = -\frac{i}{\hbar} \langle [\mathbf{J}_k, (\mathcal{H}_{\text{Ex}}(k-1) + \mathcal{H}_{\text{Ex}}(k) + \mathcal{H}_{\text{Ex}}(k+1))] \rangle. \quad (29)$$

Here, only those terms in the Hamiltonian that contain \mathbf{J}_k can contribute to the right-hand side of equation (3). On evaluating the necessary commutation relationships, for the in-plane terms we find:

$$-\frac{i}{\hbar} \langle [\mathbf{J}_k, (\mathcal{H}_{\text{Ex}}(k, k+\rho))] \rangle = \frac{\lambda_{\text{ex}}}{\hbar} \langle \mathbf{J}_k \times \mathbf{J}_{k+\rho} \rangle = 0. \quad (30)$$

Whereas for the out-of-plane terms:

$$-\frac{i}{\hbar} \langle [\mathbf{J}_k, (\mathcal{H}_{\text{Ex}}(k, k \pm 1))] \rangle = \frac{\lambda_{\text{ex}}}{\hbar} |\mathbf{J}_k \times \mathbf{J}_{k+1} + \mathbf{J}_k \times \mathbf{J}_{k-1}|. \quad (31)$$

In summary therefore:

$$\hbar \left(\frac{d}{dt} \langle \mathbf{J}_k \rangle\right)_{\text{Ex}} = \lambda_{\text{ex}} \langle \mathbf{J}_k \times \mathbf{J}_{k+1} + \mathbf{J}_k \times \mathbf{J}_{k-1} \rangle. \quad (32)$$

Turning now to the local dipolar fields (Dip) in the Cartesian reference frame:

$$\left(\frac{d}{dt}\langle J_k \rangle\right)_{\text{Dip}} = -\frac{i}{\hbar} \langle [J, -g\mu_B \mathbf{J} \cdot \mathbf{B}_{\text{Loc}}(k)]_- \rangle = \left(\frac{g\mu_B}{\hbar}\right) \langle J \rangle \times \mathbf{B}_{\text{Loc}}(k). \quad (33)$$

Here, the local dipolar field \mathbf{B}_{Loc} is given by:

$$\mathbf{B}_{\text{Loc}}(k) =$$

$$\left(\frac{\mu_0}{4\pi}\right) \left(\frac{1}{a^3}\right) \begin{pmatrix} 1 & 0 & 0 \\ 0 & 0 & 0 \\ 0 & 0 & -2 \end{pmatrix} \cdot (\mathcal{D}_{xx}^0 \boldsymbol{\mu}_k + \mathcal{D}_{xx}^1 (\boldsymbol{\mu}_{k+1} + \boldsymbol{\mu}_{k-1}) + \mathcal{D}_{xx}^2 (\boldsymbol{\mu}_{k+2} + \boldsymbol{\mu}_{k-2})). \quad (34)$$

In this equation, the dipolar constants are:

$$\mathcal{D}_{xx}^0 = 4.516811; \quad \mathcal{D}_{xx}^1 = -0.1637329; \quad \mathcal{D}_{xx}^2 = -0.000278402; \dots \quad (35)$$

These numbers are taken from [42]. Note that if all the spins are parallel:

$$\mathbf{B}_{\text{Loc}}(k) = \left(\frac{\mu_0 M}{3}\right) \begin{pmatrix} 1 & 0 & 0 \\ 0 & 1 & 0 \\ 0 & 0 & -2 \end{pmatrix} \cdot \left(\frac{\boldsymbol{\mu}}{\mu}\right). \quad (36)$$

A result, used earlier, in our discussion of a single slab.

Finally, we need to convert from the Cartesian frame into local polar coordinates. In place of the Cartesian set of vectors $(\hat{\mathbf{i}}, \hat{\mathbf{j}}, \hat{\mathbf{k}})$, we define a set of local unit vectors:

$$\widehat{\boldsymbol{\varepsilon}}\theta = \begin{pmatrix} \cos \theta \cos \phi \\ \cos \theta \sin \phi \\ -\sin \theta \end{pmatrix}; \quad \widehat{\boldsymbol{\varepsilon}}\phi = \begin{pmatrix} -\sin \phi \\ \cos \phi \\ 0 \end{pmatrix}; \quad \widehat{\boldsymbol{\varepsilon}}r = \begin{pmatrix} \sin \theta \cos \phi \\ \sin \theta \sin \phi \\ \cos \theta \end{pmatrix}. \quad (37)$$

Note: (i) $\widehat{\boldsymbol{\varepsilon}}r$ coincides with the vector \mathbf{r} (in our case a given magnetic moment $\boldsymbol{\mu}$), (ii) the unit vector $\widehat{\boldsymbol{\varepsilon}}\phi$ does not involve a change in θ (it is a rotation about the z -axis), and (iii) if we set $\theta = \phi = 0$, the set $\{\widehat{\boldsymbol{\varepsilon}}\theta, \widehat{\boldsymbol{\varepsilon}}\phi, \widehat{\boldsymbol{\varepsilon}}r\}$ coincides with the Cartesian set $(\hat{\mathbf{i}}, \hat{\mathbf{j}}, \hat{\mathbf{k}})$. Also, it is easy to show that:

$$\begin{aligned} \widehat{\boldsymbol{\varepsilon}}\theta \times \widehat{\boldsymbol{\varepsilon}}\phi &= \widehat{\boldsymbol{\varepsilon}}r. \\ \widehat{\boldsymbol{\varepsilon}}\phi \times \widehat{\boldsymbol{\varepsilon}}r &= \widehat{\boldsymbol{\varepsilon}}\theta. \\ \widehat{\boldsymbol{\varepsilon}}r \times \widehat{\boldsymbol{\varepsilon}}\theta &= \widehat{\boldsymbol{\varepsilon}}\phi. \end{aligned} \quad (38)$$

So $\{\widehat{\boldsymbol{\varepsilon}}\theta, \widehat{\boldsymbol{\varepsilon}}\phi, \widehat{\boldsymbol{\varepsilon}}r\}$ is a right-handed set of vectors. Moreover, we can easily transform between the two different sets with the unitary transformation \mathbf{U} . Explicitly:

$$\begin{pmatrix} \widehat{\boldsymbol{\varepsilon}}\theta \\ \widehat{\boldsymbol{\varepsilon}}\phi \\ \widehat{\boldsymbol{\varepsilon}}r \end{pmatrix} = \begin{pmatrix} \cos \theta \cos \phi & \cos \theta \sin \phi & -\sin \theta \\ -\sin \phi & \cos \phi & 0 \\ \sin \theta \cos \phi & \sin \theta \sin \phi & \cos \theta \end{pmatrix} \begin{pmatrix} \hat{\mathbf{i}} \\ \hat{\mathbf{j}} \\ \hat{\mathbf{k}} \end{pmatrix} = \mathbf{U} \begin{pmatrix} \hat{\mathbf{i}} \\ \hat{\mathbf{j}} \\ \hat{\mathbf{k}} \end{pmatrix}. \quad (39)$$

All the above is in agreement with Varshalovich *et al* [50].

The final step involves ‘linearization’. Following Van Vleck [36] and Nörtemann *et al* [37], we set:

$$\mathbf{J}_k \rightarrow \mathbf{J}_k^0 + \mathbf{j}_k. \quad (40)$$

Here \mathbf{j}_k is a small, time-dependent variation about the DC component \mathbf{J}_k^0 . In terms of local coordinates:

$$\mathbf{j}_k = J \left(\partial\theta_k \widehat{\boldsymbol{\varepsilon}}\theta + \sin \theta_k \partial\phi_k \widehat{\boldsymbol{\varepsilon}}\phi \right), \quad (41)$$

i.e. small orthogonal rotations of the spin about its equilibrium position. Proceeding in this manner, we find, after some manipulation, that the dynamical equations can be expressed in the matrix form:

$$(i\omega \mathbf{I} - \mathcal{M}) \Psi = 0 \quad \text{or} \quad (\omega \mathbf{I} + i\mathcal{M}) \Psi = 0. \quad (42)$$

Here Ψ is a column matrix containing the $\partial\theta_k, \sin \theta_k \partial\phi_k$ ($k = 1, N$) amplitudes, where N is the number of layers, and \mathcal{M} is a $2N \times 2N$ matrix. Thus, the resonance frequencies ω are given by the eigenvalues of

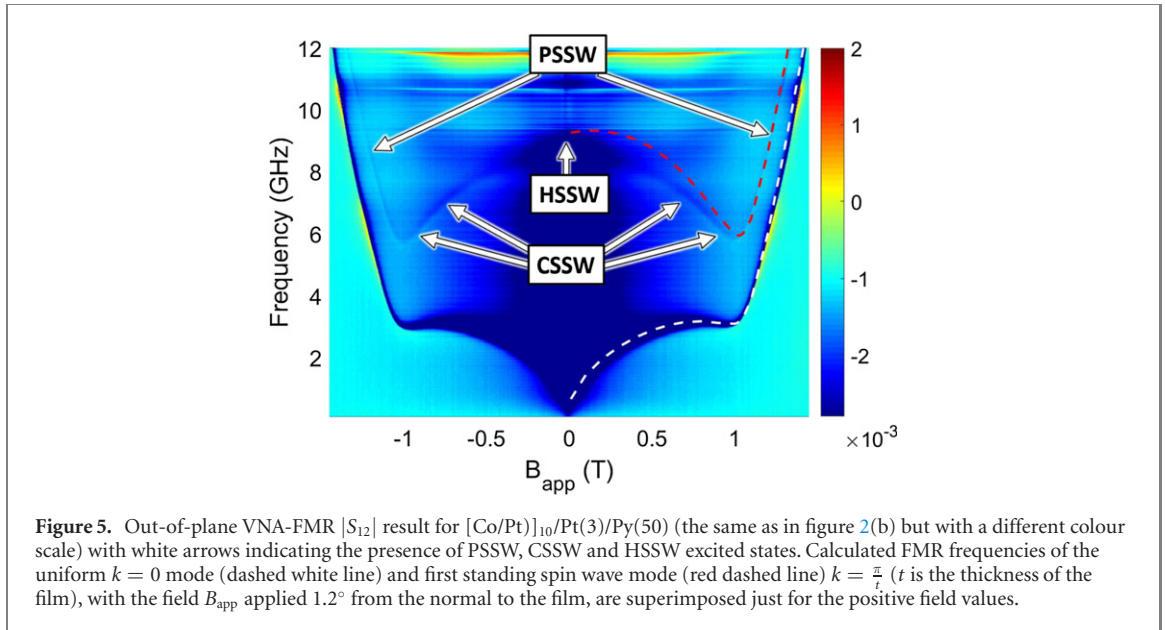


Figure 5. Out-of-plane VNA-FMR $|S_{12}|$ result for $[\text{Co/Pt}]_{10}/\text{Pt}(3)/\text{Py}(50)$ (the same as in figure 2(b) but with a different colour scale) with white arrows indicating the presence of PSSW, CSSW and HSSW excited states. Calculated FMR frequencies of the uniform $k = 0$ mode (dashed white line) and first standing spin wave mode (red dashed line) $k = \frac{\pi}{t}$ (t is the thickness of the film), with the field B_{app} applied 1.2° from the normal to the film, are superimposed just for the positive field values.

$\mathcal{U}(i\mathcal{M})\mathcal{U}^{-1}$, where \mathcal{U} is a similarity transformation. In passing, we also note the matrix \mathcal{M} is gyroscopic, with eigenvalues of the form $\pm\hbar\omega_k$. This has to be the case, given that the solution must hold for spins with a different sign for the gyromagnetic constant γ .

6. Excited states in Py films

In figure 5 an expanded diagram of the VNA-FMR diagram of figure 2(b) can be seen, with arrows indicating the presence of PSSW, CSSW, and HSSW excited states.

In applied fields $B_{\text{app}}^x > \mu_0 M$ (~ 1 T), a faint straight line is evident, running parallel to the principle $k = 0$ uniform mode, but shifted upwards in frequency by about 2.6 GHz (it is especially evident in figures 2(b) and (c)). This is a characteristic feature of a PSSW state [6]. In fields exceeding 1.02 T, the spins point normal to the film. However, *pinning* on the top and bottom of the film leads to a half-wavelength excitation:

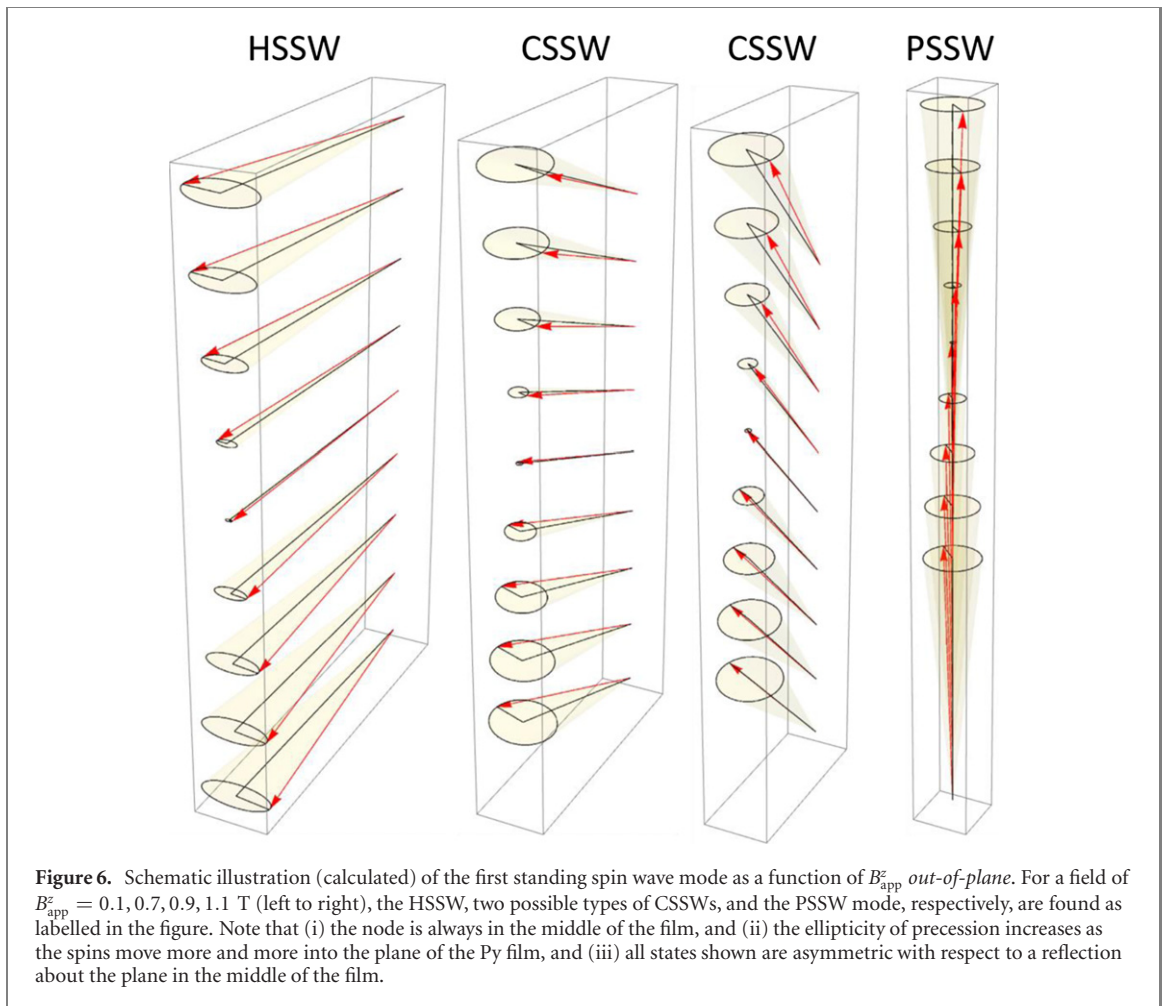
$$h\nu = h\nu_0 + Dk^2. \quad (43)$$

Here, (i) $h\nu_0$ is the energy associated with the uniform mode, and (ii) $k = \frac{\pi}{t}$ ($\lambda = 2t$), where t is the thickness of the film. Thus, in fields exceeding 1.02 T, the PSSW (M_\perp) mode should run parallel to the normal mode, but shifted upwards by Dk^2 . Using Weber's Py results for a 500 nm film, we find $D = 6.14 \times 10^{-7}$ Hz m² and $\mu_0 M = 1.053$ T (see also appendix B of Bowden *et al* [51]). With these figures, the calculated upwards frequency shift of the PPSW mode is 2.63 GHz for a 50 nm Py film. This estimate agrees well with the data in figure 5.

With the aid of the Py multilayer model of section 5, it is possible to calculate, not only the normal $k = 0$ mode, but also all the excited states. In figure 5, we show the calculated normal mode and the first excited state, in a Py(50) film, with (i) the field applied 1.2° off the film *normal*, and (ii) no artificial surface *pinning*, other than the fact that the local dipolar field for the top and bottom layers differs from those in the bulk by $\sim 5\%$. The strength of the Py exchange interaction λ_{ex} was adjusted to give a splitting of 2.63 GHz between the normal mode ($k = 0$) and the PSSW, above 1.02 T, in the out-of-plane results (see the two straight lines in figure 1). The number of layers used for the 50 nm-thick Py film was set at $N = 188$ and $\lambda_{\text{ex}} = 214$ K. For clarity, the calculated data are superimposed on the experimental data only for positive magnetic field values. The comparison shows that there is very reasonable agreement between the experiment and theory. Clearly, the PSSW morphs into an HSSW of some sort, cutting the frequency axis at ~ 9.3 GHz.

The multilayer model not only gives the frequencies of all the excited states but also their eigenvectors. A schematic picture of the *in-plane* HSSW and *out-of-plane* PSSW excited states, and the transition between the two, can be seen in figure 6.

Note that the excited states are characterised by (i) a node in the middle of the film, and (ii) maximum displacements at the top and bottom of the film, but phase shifted by 180° with respect to each other (asymmetric). Moreover, for the higher energy modes, the multi-layer model predicts two stationary nodes,

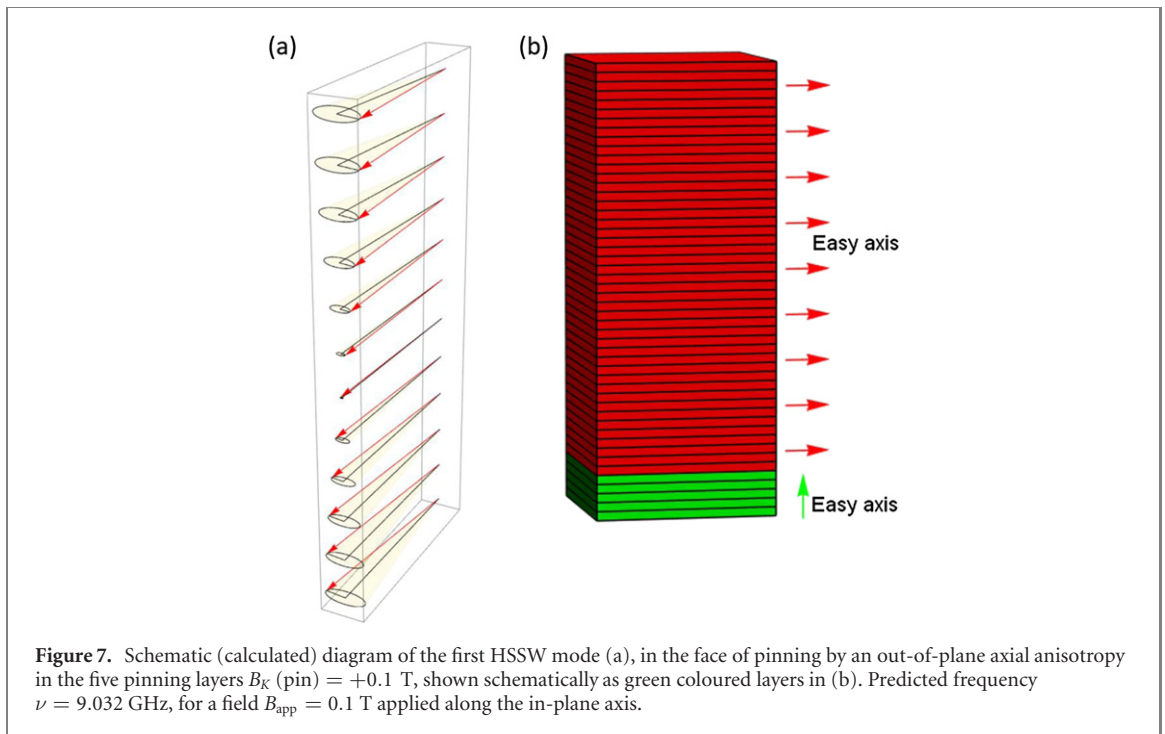


three nodes etc, all inside the film. All of the states are characterized by $\lambda_1 = 2t, \lambda_2 = t, \lambda_3 = \frac{2t}{3}$ etc. In particular, none of the calculated modes shows pinning at the surfaces of the film. The same is also true for the calculated PSSW modes above 1.0 T. The results of the multilayer model therefore suggest that the rf excitation field must be non-uniform across the magnetic film thickness [23–28]. This situation is examined in more detail in the following section. However, in passing we note two things. Firstly, the HSSW state shown in figure 5 (9.3 GHz in zero applied field) is the same as that obtained when the field is applied *in-plane*, and reduced to zero. Secondly, the frequency of the HSSW state in zero field (9.3 GHz) is much greater than that of the PSSW (2.63 GHz) despite both states being characterized by a wavelength $\lambda = 2t$. This difference in frequency is due entirely to the action of the demagnetization field, normal to the plane of the film, which forces the precession of the spins into an elliptical orbit. Indeed, an explicit equation for the ellipticity of precession is readily obtained, using Kittel's equation for a single slab with the applied field *in-plane*:

$$\varepsilon = \sqrt{\left(\frac{B_{\text{app}} + B_K + \mu_o M}{B_{\text{app}} + B_K}\right)}. \quad (44)$$

Note that $\varepsilon \rightarrow 1$ when $\mu_o M \rightarrow 0$. This is equivalent to *switching-off* the demagnetization field. The ellipticity is also unity for *out-of-plane* fields, when $B_{\text{app}}^z > \mu_o M + B_K$.

Finally, we note that the above results represent the first observation of the transition between PSSW and HSSW modes in extended thin films by FMR. Similar dispersions of SSW states have been observed in laterally structured ferromagnets such as Py wires [52–54]. However, due to the confined geometry of the nanostructures, the PSSWs are often obscured by the presence of additional spin waves modes such as quantized magnetostatic forward volume modes and dipole-exchange modes [54].

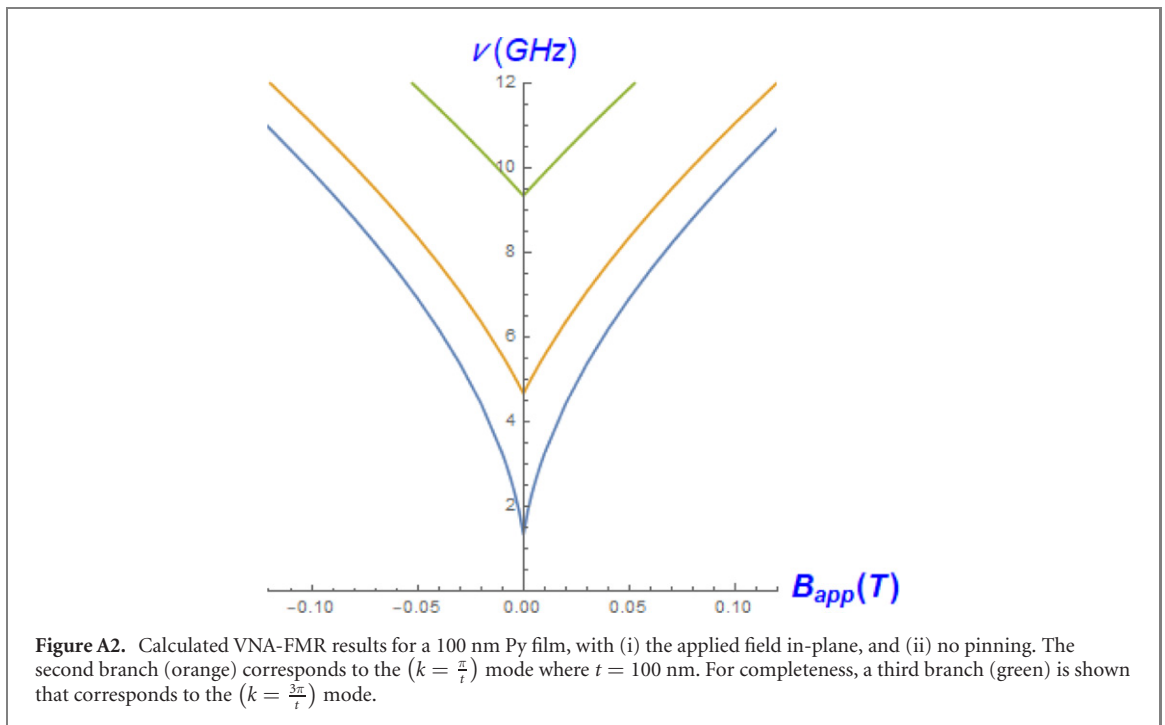
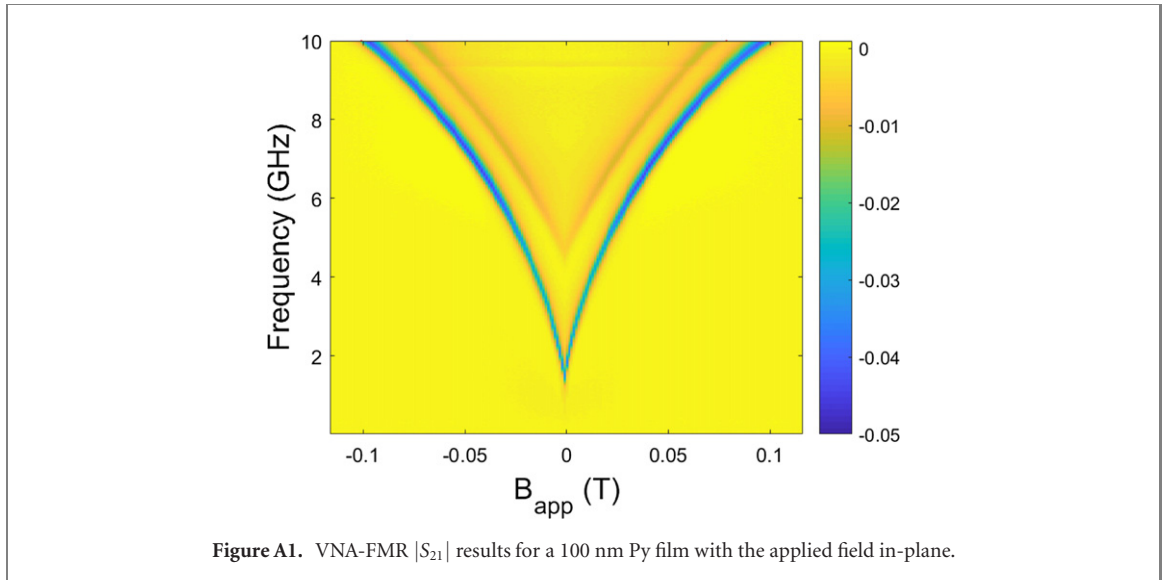


7. Excitation of asymmetric SSW states

The excitation of antisymmetric spin-waves states has attracted much attention [25–28]. In particular, calculations by Kostylev [26] show that the in-plane dynamic rf-field at a given thickness of the film is generated, primarily, by two components: (i) the primary rf-exciting field, from the CPW, and (ii) a secondary rf-field, generated by the eddy currents in the film. These two contributions give rise to an overall asymmetric rf-field, with (i) a much reduced skin depth, than simple calculations would suggest, and (ii) the potential to excite asymmetric SSW modes (see for example figure 2(c) in reference [26], and subsequent discussion). In addition, pinning at one of the surfaces can also induce asymmetry. Clearly, given that the Py layers sit atop a [Co/Pt] layer, characterized by perpendicular anisotropy, such a situation exists in this work. However, here, we must urge caution. Firstly, if the Pt spacer exceeds 1.5 nm, the Py film is effectively magnetically decoupled from the [Co/Pt] layer (see figure 3(b)). Secondly, even when the Pt spacer is removed, both the in-plane and out-of-plane Py/FMR results, basically follow the Kittel-like behaviour. Nonetheless, asymmetry in the samples is present, together with asymmetry in the effective rf-field. Thus, asymmetric SSW-states can be excited, and witnessed [25].

Given the multi-layer Py model, discussed in section 6, it is a relatively easy matter to examine the effects of pinning by the [Co/Pt] layer. Here, we briefly discuss a simple model, where the [Co/Pt] layer is replaced by an extra 5 layers of Py, but with an anisotropy which favours the normal to the film, specifically to $B_K(\text{pin}) = +0.1$ T, shown schematically in figure 7(b). Here, the frequency of the uniform mode decreases from $\nu = 1.5$ to 0.991 GHz, while that of the first standing spin wave mode increases to $\nu = 9.032$ GHz. In this example, the amplitude of precession of the uniform mode increases by some 15%, as the pinning layer is approached (not shown). This is understandable, given that the bulk of the Py film wishes to remain in-plane, while pinning layers want to point out-of-plane. A schematic picture of the first excited state can be seen in figure 7(a). Note the definite movement of the node towards the pinning layer (bottom).

Thus, the mode in question is no longer purely antisymmetric. In principle therefore, even a uniform rf-field can excite such a mode. However, as described in appendix A, VNA-FMR results on a 100 nm Py film, deposited directly on top of a MgO substrate, show clear evidence of an excited HSSW state. In this case, it is hard not to accept that such states must be driven by an asymmetric rf-field (see e.g. reference [26]). Note that the in-plane magnetic anisotropy and in-plane magnetic field (as in appendix A), there is no need to differentiate between HSSW, CSSW and PSSW modes as the magnetization remains always in the sample plane, and such states are commonly defined as PSSW modes in the literature.



Note also that for the directly coupled [Co/Pt]/Py structures, no evidence of PSSWs can be observed (see figure 2(d)), even though the pinning at the bottom Py interface is expected to be strongest for this sample. The absence of PSSWs for the [Co/Pt]/Py sample may be due to the formation of a domain structure within the Py layer [43].

Finally, it should be acknowledged that the above theory could be generalized to include Pincus modes (Pincus 1960 [55], see also Kishine *et al* [56]). Here, *soft* surface pinning at the top and bottom of a film, magnetized perpendicular to the film, allows excitation of *asymmetric* PSSW modes in uniform rf-fields. Such Pincus modes require the Larmor frequency of the surface spins to match that of PSSW excited state. Clearly, this is an avenue for further exploration. For example, one can ask the question: can Pincus modes be extended to include CSSW states? Indeed, this may not be possible, given that both the effective anisotropy, and energy of the CSSW state change, as magnetic moments move progressively into the plane of the film.

8. Conclusions and discussion

In this paper, both FMR and XFMR results for Py and [Co/Pt]/Py films have been presented and discussed. In general, the FMR results appear to be dominated by the Py film, showing little in the way of polarization by the underlying [Co/Pt] multilayer. In particular, by using XFMR, we have demonstrated that the dynamic coupling between [Co/Pt] and Py layers is completely suppressed when separated by a 1.5 nm thick Pt spacer layer. Most importantly, we have shown that out-of-plane VNA-FMR maps reveal the presence of standing spin waves modes in the whole investigated magnetic field range. For example, a PSSW state, with $\lambda = 2t$, above the cusp at $B_{\text{app}}^z \gtrsim \mu_0 M$, has been clearly identified. Moreover, as the magnetic field is reduced below $\mu_0 M$, this state morphs, continuously, via a series of CSSW states, and, eventually into an in-plane HSSW state, which increases in frequency to ~ 9.5 GHz. All of the PSSW, CSSW and HSSW modes are characterized by $\lambda = 2t$, but differ significantly in frequency. This is primarily due to the demagnetization factor of -1 associated with a thin film. For fields applied out-of-plane, the magnetic field *seen* by the Py spins is given by $B_{\text{eff}} = B_{\text{app}} - \mu_0 M$. However, as the field is reduced, the spins move increasingly into the plane of the film, where the effective field is given by $B_{\text{eff}} = \sqrt{(B_{\text{app}} + |B_K|)(B_{\text{app}} + |B_K| + \mu_0 M)}$. Here, the diminution of the applied field is more than made up by the contribution originating from $\mu_0 M$. Finally, the observed VNA-FMR results for both $k = 0$ and $k \neq 0$ have been interpreted using a multi-layer Py film model, based on (i) the linearization procedure of Van Vleck [36] and Nörtemann *et al* [37], and (ii) the local-dipolar field model for thin films (Bowden *et al* [51]). Finally, our results provide better understanding of CSSW modes and should be of particular interest for MAMR, where CSSW modes may be optimized to reduce the energy required to reorient the magnetization.

Data availability statement

The data that support the findings of this study are available upon reasonable request from the authors.

Acknowledgments

The authors acknowledge the Engineering and Physical Sciences Research Council (EPSRC) under Grant No. EP/P021190/1, EP/P020151/1, and EP/P02047X/1. This research used resources of the Advanced Light Source, which is a DOE Office of Science User Facility under Contract No. DE-AC02-05CH11231. DGN acknowledges support via the EPSRC Centre for Doctoral Training in Metamaterials (Grant No. EP/L015331/1). We acknowledge Prof Takafumi Nakano for the loan of the 100 nm Py film discussed in appendix A.

Appendix A

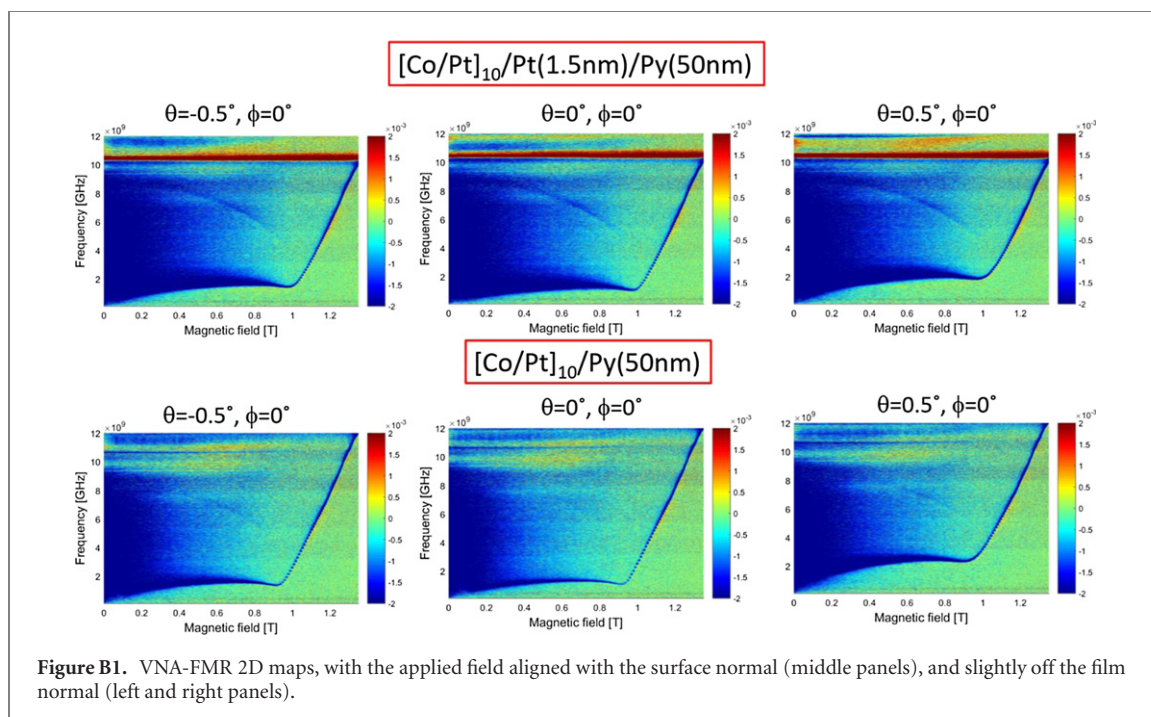
In-plane VNA-FMR results for the 100 nm-thick Py film, grown directly onto a MgO substrate, can be seen in figure A1. Here, the FMR ($k = 0$) mode faithfully follows the predictions of the Kittel formula of equation (1), with clear evidence of an in-plane anisotropy field B_K . However, there is clear evidence of a second branch some 4 GHz above the ($k = 0$) mode.

This second branch ($k = \frac{\pi}{t}$) can be well-interpreted using the parameters of the multilayer Py model presented in section 5, except for the thickness t . The calculated results, for a 100 nm film, can be seen in figure A2. This second branch is an HSSW state (or simply the PSSW state, as there are no other states present since the magnetization always remains in the sample plane in the current geometry), similar in nature to that shown in the left-hand side of figure 6.

Finally, we note that this 100 nm Py film is essentially *unpinned* both top and bottom. Thus, excitation of the excited state must be driven by an asymmetric rf-field (e.g. reference [35]).

Appendix B. Effect of the field misalignment on the VNA-FMR of [Co/Pt]/Py(50) and [Co/Pt]/Pt(1.5)/Py(50) samples.

From an examination of the above VNA-FMR results, we conclude that small misalignments can shift the frequency of the *cusp* in the $k = 0$ FMR curve. However, in general, we were not able to bring the *cusp* down to zero frequency. Note also the clear presence of the CSSW states, between the PSSW and HSSW states, in the top three diagrams (figure B1).



ORCID iDs

Maciej Dąbrowski  <https://orcid.org/0000-0002-6033-5721>

Andreas Frisk  <https://orcid.org/0000-0001-9234-0907>

David G Newman  <https://orcid.org/0000-0002-4076-0288>

Thorsten Hesjedal  <https://orcid.org/0000-0001-7947-3692>

References

- [1] Griffiths J H E 1946 Anomalous high-frequency resistance of ferromagnetic materials *Nature* **158** 670
- [2] Kittel C 1946 Theory of the dispersion of magnetic permeability of ferromagnetic materials at microwave frequencies *Phys. Rev.* **70** 281
- [3] Kittel C 1948 On the theory of ferromagnetic absorption *Phys. Rev.* **73** 155
- [4] Kittel C 1951 Ferromagnetic resonance *J. Phys. Radium* **12** 291
- [5] Kittel C 1974 *Introduction to Solid State Physics* 4th edn (New York: Wiley)
- [6] Weber R 1968 Spin-wave resonance *IEEE Trans. Magn.* **4** 28
- [7] Phillips T G and Rosenberg H M 1966 Spin waves in ferromagnets *Rep. Prog. Phys.* **29** 285
- [8] Frait Z and Fraitova D 1988 *Spin-Wave Resonance in Metals Modern Problems in Condensed Matter Sciences* vol 22 (Amsterdam: North-Holland) pp 1–65
- [9] Slavin A and Tiberkevich V 2005 Spin wave mode excited by spin-polarized current in a magnetic nanocontact is a standing self-localized wave *Phys. Rev. Lett.* **95** 237201
- [10] Bonetti S, Tiberkevich V, Consolo G, Finocchio G, Muduli P, Mancoff F, Slavin A and Åkerman J 2010 Experimental evidence of self-localized and propagating spin wave modes in obliquely magnetized current-driven nanocontacts *Phys. Rev. Lett.* **105** 217204
- [11] Chumak A V, Vasyuchka V I, Serga A A and Hillebrands B 2015 Magnon spintronics *Nat. Phys.* **11** 453
- [12] Unwin M E, Haycock P W, Hoon S R and Grannell P K 1999 Novel broadband ferromagnetic resonance spectrometer *J. Magn. Mater.* **205** 199
- [13] Qin H, Hämäläinen S J and van Dijken S 2018 Exchange-torque-induced excitation of perpendicular standing spin waves in nanometer-thick YIG films *Sci. Rep.* **8** 5755
- [14] Klingler S et al 2018 Spin-torque excitation of perpendicular standing spin waves in coupled YIG/Co heterostructures *Phys. Rev. Lett.* **120** 127201
- [15] Marcham M K et al 2013 Phase-resolved x-ray ferromagnetic resonance measurements of spin pumping in spin valve structures *Phys. Rev. B* **87** 180403
- [16] van der Laan G and Figueroa A I 2014 X-ray magnetic circular dichroism—a versatile tool to study magnetism *Coord. Chem. Rev.* **277–278** 95
- [17] Burn D M, Zhang S L, Yu G Q, Guang Y, Chen H J, Qiu X P, van der Laan G and Hesjedal T 2020 Depth-resolved magnetization dynamics revealed by x-ray reflectometry ferromagnetic resonance *Phys. Rev. Lett.* **125** 137201
- [18] Burn D M, Zhang S, Zhai K, Chai Y, Sun Y, van der Laan G and Hesjedal T 2019 Mode-resolved detection of magnetization dynamics using x-ray diffractive ferromagnetic resonance *Nano Lett.* **20** 345
- [19] Dąbrowski M et al 2020 Coherent transfer of spin angular momentum by evanescent spin waves within antiferromagnetic NiO *Phys. Rev. Lett.* **124** 217201

- [20] Bonetti S *et al* 2015 Microwave soft x-ray microscopy for nanoscale magnetization dynamics in the 5–10 GHz frequency range *Rev. Sci. Instrum.* **86** 093703
- [21] Perzlmaier K, Buess M, Back C H, Demidov V E, Hillebrands B and Demokritov S O 2005 Spin-wave eigenmodes of permalloy squares with a closure domain structure *Phys. Rev. Lett.* **94** 057202
- [22] Park J P and Crowell P A 2005 Interactions of spin waves with a magnetic vortex *Phys. Rev. Lett.* **95** 167201
- [23] Khivintsev Y V, Reisman L, Lovejoy J, Adam R, Schneider C M, Camley R E and Celinski Z J 2010 Spin wave resonance excitation in ferromagnetic films using planar waveguide structures *J. Appl. Phys.* **108** 023907
- [24] Schoen M A W, Shaw J M, Nembach H T, Weiler M and Silva T J 2015 Radiative damping in waveguide-based ferromagnetic resonance measured via analysis of perpendicular standing spin waves in sputtered permalloy films *Phys. Rev. B* **92** 184417
- [25] Crew D C, Kennewell K J, Lwin M J, Woodward R C, Prasad S and Stamps R L 2005 Optic and acoustic modes measured in a cobalt/permalloy exchange spring bilayer using inductive magnetometry *J. Appl. Phys.* **97** 10A707
- [26] Kostylev M 2009 Strong asymmetry of microwave absorption by bilayer conducting ferromagnetic films in the microstrip-line based broadband ferromagnetic resonance *J. Appl. Phys.* **106** 043903
- [27] Kostylev M 2013 Waveguide-based ferromagnetic resonance measurements of metallic ferromagnetic films in transmission and reflection *J. Appl. Phys.* **113** 053908
- [28] Kennewell K J 2008 Surface and interface anisotropies measured using inductive magnetometry *PhD Thesis* University of Western Australia
- [29] Magaraggia R, Kennewell K, Kostylev M, Stamps R L, Ali M, Greig D, Hickey B J and Marrows C H 2011 Exchange anisotropy pinning of a standing spin-wave mode *Phys. Rev. B* **83** 054405
- [30] Rzdolski I, Alekhin A, Ilin N, Meyburg J P, Roddatis V, Dising D, Bovensiepen U and Melnikov A 2017 Nanoscale interface confinement of ultrafast spin transfer torque driving non-uniform spin dynamics *Nat. Commun.* **8** 15007
- [31] Zhou W, Seki T, Iwama H, Shima T and Takanashi K 2015 Perpendicularly magnetized $L1_0$ -FePt nanodots exchange-coupled with soft magnetic $Ni_{81}Fe_{19}$ *J. Appl. Phys.* **117** 013905
- [32] Seki T, Utsumiya K, Nozaki Y, Imamura H and Takanashi K 2013 Spin wave-assisted reduction in switching field of highly coercive iron-platinum magnets *Nat. Commun.* **4** 1726
- [33] Zhou Y, Zha C L, Bonetti S, Persson J and Åkerman J 2008 Spin-torque oscillator with tilted fixed layer magnetization *Appl. Phys. Lett.* **92** 262508
- [34] Devolder T, Couet S, Swerts J and Kar G S 2018 Gilbert damping of high anisotropy Co/Pt multilayers *J. Phys. D: Appl. Phys.* **51** 135002
- [35] Nguyen T N A *et al* 2014 Depth-dependent magnetization profiles of hybrid exchange springs *Phys. Rev. Appl.* **2** 044014
- [36] Van Vleck J H 1950 Concerning the theory of ferromagnetic resonance absorption *Phys. Rev.* **78** 266
- [37] Nörtemann F C, Stamps R L and Camley R E 1993 Microscopic calculation of spin waves in antiferromagnetically coupled multilayers: nonreciprocity and finite size effects *Phys. Rev. B* **47** 11910
- [38] Gurevich A G and Melkov G A 1996 *Magnetization Oscillations and Waves* (Boca Raton, FL: CRC Press)
- [39] Gilbert T L 2004 A phenomenological theory of damping in ferromagnetic materials *IEEE Trans. Magn.* **40** 3443
- [40] Smit J and Beljers H G 1955 Ferromagnetic resonance absorption in $BaFe_{12}O_{19}$, a highly anisotropic crystal *Philips Res. Rep.* **10** 113
- [41] Farle M 1998 Ferromagnetic resonance of ultrathin metallic layers *Rep. Prog. Phys.* **61** 755
- [42] Bowden G J, Stenning G B G and van der Laan G 2016 Asymptotic behavior of local dipolar fields in thin films *J. Magn. Mater.* **416** 449
- [43] Dąbrowski M *et al* 2020 Optically and microwave-induced magnetization precession in [Co/Pt]/NiFe exchange springs *ACS Appl. Mater. Interfaces* **12** 52116
- [44] van der Laan G 2017 Time-resolved x-ray detected ferromagnetic resonance of spin currents *J. Electron Spectrosc. Relat. Phenom.* **220** 137
- [45] Klewe C *et al* 2020 Element- and time-resolved measurements of spin dynamics using x-ray detected ferromagnetic resonance *Synchrotron Radiat. News* **33** 12
- [46] Kuan B K, Lopusnik R, Malkinski L M, Wenger M, Yu M, Scherer D II, Camley R E and Celinski Z 2008 High frequency characterization of Permalloy nanosized strips using network analyser ferromagnetic resonance *J. Appl. Phys.* **103** 07C508
- [47] Tannewald P E and Seavey M H 1957 Ferromagnetic resonance in thin films of Permalloy *Phys. Rev.* **103** 377
- [48] Utsumiya K, Seki T and Takanashi K 2011 Magnetic properties of $L1_0$ -FePt/Permalloy exchange-spring films *J. Appl. Phys.* **110** 103911
- [49] Bowden G J, Beaujour J-M L, Zhukov A A, Rainford B D, de Groot P A J, Ward R C C and Wells M R 2003 Modelling the magnetic properties of $DyFe_2/YFe_2$ superlattices *J. Appl. Phys.* **93** 6480
- [50] Varshalovich D A, Moskalev A N and Khersoskii V K 1988 *Quantum Theory of Angular Momentum* (Singapore: World Scientific)
- [51] Bowden G J, van der Laan G, Hesjedal T and Hicken R J 2019 Expanding the Lorentz concept in magnetism *New J. Phys.* **21** 073063
- [52] Nguyen T M, Cottam M G, Liu H Y, Wang Z K, Ng S C, Kuok M H, Lockwood D J, Nielsch K and Gösele U 2006 Spin waves in Permalloy nanowires: the importance of easy-plane anisotropy *Phys. Rev. B* **73** 140402
- [53] Tartakovskaya E V 2005 Quantized spin-wave modes in long cylindrical ferromagnetic nanowires in a transverse external magnetic field *Phys. Rev. B* **71** 180404
- [54] Gui Y S, Mecking N and Hu C-M 2007 Quantized spin excitations in a ferromagnetic microstrip from microwave photovoltage measurements *Phys. Rev. Lett.* **98** 217603
- [55] Pincus P 1960 Excitation of spin-waves in ferromagnets: eddy currents and boundary conditions *Phys. Rev.* **118** 658
- [56] Kishine J, Sinitsyn V I E, Bostrem J G, Proskurin I, Goncalves F J T, Togawa Y and Ovchinnikov A S 2019 Theory of standing spin-waves in a finite size chiral spin soliton lattice *Phys. Rev. B* **100** 024411